3660 Biophysical Journal Volume 89 November 2005 3660–3668

Extracellular Space Diffusion in Central Nervous System: Anisotropic Diffusion Measured by Elliptical Surface Photobleaching

Marios C. Papadopoulos, Jung Kyung Kim, and A. S. Verkman
Departments of Medicine and Physiology, Cardiovascular Research Institute, University of California, San Francisco, California 94143

ABSTRACT Diffusion in the extracellular space (ECS) is crucial for normal central nervous system physiology. The determinants of ECS diffusion include viscous interactions with extracellular matrix/plasma membranes ("viscosity") and ECS geometry ("tortuosity"). To resolve viscosity versus tortuosity effects, we measured direction-dependent (anisotropic) diffusion in ECS in mouse spinal cord by photobleaching using an elliptical spot produced by a cylindrical lens in the excitation path. Anisotropic diffusion slowed fluorescence recovery when the long axis of the ellipse was parallel versus perpendicular to the direction of faster diffusion. A mathematical model was constructed to deduce diffusion coefficients (D_x, D_y) from fluorescence recovery measured for parallel and perpendicular orientations of the long axis of the ellipse. Elliptical spot photobleaching was validated by photobleaching aqueous-phase fluorophores on a diffraction grating, where diffusion is one-dimensional. Measurement of the diffusion of 70 kDa FITC-dextran in spinal cord in living mice indicated that viscosity slows diffusion by ~1.8-fold compared with its diffusion in solution. ECS geometry hinders diffusion across (but not along) axonal fibers in spinal cord further by approximately fivefold. In cerebral cortex, however, ~50% of the hindrance to ECS diffusion comes from viscosity and ~50% from tortuosity. We suggest that the extracellular matrix might have evolved to facilitate rather than hinder diffusion even for large molecules.

INTRODUCTION

The extracellular space (ECS) in the central nervous system (CNS) comprises ~20% of total tissue volume, consisting of a jelly-like matrix in which neurons, glia, and blood vessels are embedded. Diffusion of solutes and macromolecules in the ECS is vital for many CNS functions, including extrasynaptic intercellular communication, delivery of substrates and drugs to cells, elimination of metabolites, and buffering of extracellular ions (1,2). Altered ECS diffusion produced by brain edema, astrogliosis, brain tumor, and ischemia is therefore potentially detrimental (3–8).

Most studies of ECS diffusion have used the tetramethylammonium (TMA^+) technique, which involves pulsed iontophoretic introduction of TMA^+ and microelectrode measurement of decreasing TMA^+ concentration as TMA^+ diffuses away from the injection site (9). However, the TMA^+ method is largely restricted to brain slices, requires micropipette invasion of the recording site, and can only detect TMA^+. We recently developed a spot photobleaching approach to overcome these limitations, in which the ECS is fluorescently stained for in vivo measurement of diffusion by photobleaching (3).

Here, we report a novel adaptation to the photobleaching method, called ''elliptical spot photobleaching'', to measure direction-dependent diffusion coefficients in anisotropic environments. Elliptical spot photobleaching was applied to determine the relative contributions of ECS geometry (''tortuosity'') versus viscous interactions between the probe and extracellular matrix (ECM)/plasma membranes (''viscosity'') in hindering diffusion in ECS. The role of ECS tortuosity versus viscosity highlighted by Rusakov and Kullmann (10) has been widely discussed (1,9,11) and modeled mathematically (10,12), but has not been subject to experimental evaluation. Our approach to measure anisotropic diffusion, as diagrammed in Fig. 1 *A*, was to introduce directionality into the photobleaching measurement using an elliptical spot produced by cylindrical excitation optics. After photobleaching an elliptical spot, fluorescent molecules diffuse into the bleached area from the surrounding region. The time evolution of fluorophore concentration $C(x, y, t)$ is described by the diffusion equation: $\partial C/\partial t = D_x \cdot \partial^2 C/\partial x^2 + D_y \cdot \partial^2 C/\partial y^2$, where D_x and D_y are fluorophore diffusion coefficients in the *x*- and *y*-directions, respectively. If diffusion is greater in the *y*-direction than the *x*-direction ($D_y > D_x$), then fluorescence recovery is faster when the long axis of the ellipse is oriented in the *x*-direction. Recovery is independent of ellipse orientation when diffusion is isotropic ($D_x = D_y$). This two-dimensional (2D) analysis ignores the contribution of diffusion along the *z*-direction (D_z) to fluorescence recovery. In the Supplementary Material, we solve the problem in three-dimensional (3D) and show that ignoring D_z does not appreciably influence the estimates of D_x and D_y.

Submitted June 6, 2005, and accepted for publication August 15, 2005.

Marios C. Papadopoulos and Jung Kyung Kim contributed equally to this work.

Address reprint requests to Alan S. Verkman, MD, PhD, 1246 Health Sciences East Tower, Cardiovascular Research Institute, University of California, San Francisco, CA 94143-0521. Tel.: 415-476-8530; Fax: 415-665-3847; E-mail: verkman@itsa.ucsf.edu; http://www.ucsf.edu/verklab.

Abbreviations used: ECS, extracellular space; aCSF, artificial cerebrospinal fluid; ECM, extracellular matrix; FITC, fluorescein isothiocyanate; TMA^+, tetramethylammonium.

0006-3495/05/11/3660/09 $2.00

doi: 10.1529/biophysj.105.068114

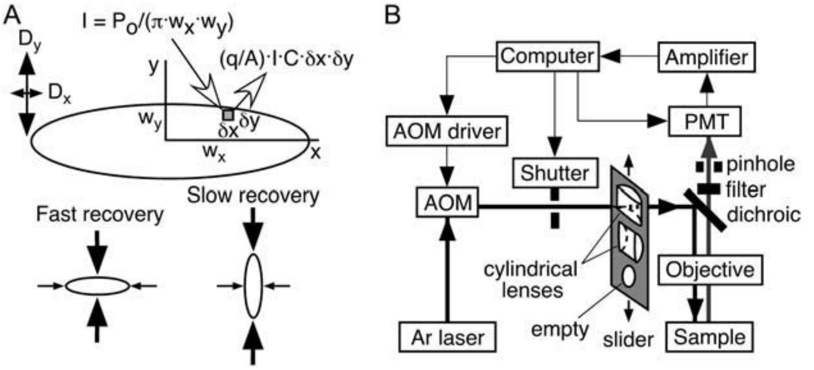

FIGURE 1 Theory and apparatus for elliptical spot photobleaching. (*A*, *top*) Ellipse with radii w_x and w_y orientated along the x and y axes, respectively. After photobleaching fluorophores with diffusion coefficients D_x and D_y ($D_x < D_y$ shown) enter the elliptical detection region. Fluorophore concentration at time t is $C(x, y, t)$ at position (x, y). Excitation light intensity is $I(x, y) = P_0/(\pi \cdot w_x \cdot w_y)$ inside the ellipse and $I(x, y) = 0$ outside, and emitted fluorescence intensity is $(q/A) \cdot I(x, y) \cdot C(x, y, t)\, \delta x \cdot \delta y$, where P_0 is laser power, q is the product of all the quantum efficiencies of light absorption, emission and detection, and A is the attenuation factor of the beam during observation of recovery. See Theory section for details. (*A*, *bottom*) Fluorescence recovery after photobleaching is faster when the long axis of the ellipse is perpendicular versus parallel to the direction of greatest diffusion. (*B*) Schematic of apparatus. AOM, acousto-optic modulator; PMT, photomultiplier. The slider allows introduction of cylindrical lenses into the excitation path.

We measured the diffusion of an inert macromolecule in the ECS of spinal white matter, reasoning that ECS diffusion along axons should depend primarily on viscosity and not on tortuosity, whereas diffusion perpendicular to axons is reduced by both viscosity and tortuosity. Diffusion was also measured in the ECS of cerebral cortex, which is hindered by both viscosity and tortuosity. We found that both viscosity and tortuosity slow diffusion: viscosity reduces diffusion ~1.8-fold (compared to water); tortuosity reduces diffusion further by approximately fivefold across white matter tracts and by ~1.8-fold in CNS gray matter.

THEORY

An analytical solution to the problem of relating diffusion coefficients to elliptical spot photobleaching data is derived below for 2D diffusion. A Monte-Carlo numerical solution for the 3D case revealed that the 2D analysis provides an excellent approximation to the 3D problem (see Supplementary Material and Fig. 3 *A*). We have therefore used the 2D analysis to interpret the data. Anisotropic diffusion in 2D is described by,

$$\frac{\partial C(x,\,y,\,t)}{\partial t} = D_x \frac{\partial^2 C(x,\,y,\,t)}{\partial x^2} + D_y \frac{\partial^2 C(x,\,y,\,t)}{\partial y^2}, \qquad (1)$$

where D_x and D_y are diffusion coefficients along the x and y axes, respectively, and $C(x, y, t)$ is fluorophore concentration at a position (x, y) and time t. The Green's function, $G(x, y, x', y', t, 0)$, gives the concentration of diffusing molecules at position (x, y) and time t due to a point source at a position (x', y') at time 0 (13),

$$G(x,y,x',y',t,0) = \frac{1}{4\pi t\sqrt{D_x D_y}} \exp\left[-\frac{(x-x')^2}{4D_x t} - \frac{(y-y')^2}{4D_y t}\right]. \qquad (2)$$

$C(x, y, t)$ is obtained by integrating $G(x, y, x', y', t, 0)$ over (x', y'), with the initial distribution of the diffusing molecules $C(x', y', 0)$,

$$C(x,y,t) = \int_{-\infty}^{\infty}\int_{-\infty}^{\infty} C(x',y',0)G(x,y,x',y',t,0)dx'dy'. \qquad (3)$$

We assume an initially uniform fluorophore concentration C_0 and that bleaching is an irreversible first-order reaction: $dC/dt = -\alpha I(x, y)C$, where $I(x, y)$ is the bleach intensity. Initial fluorophore concentration in the bleached area with bleach pulse of time duration T is thus: $C(x, y, 0) = C_0\exp[-\alpha T I(x, y)]$. For a uniform elliptic bleach spot, $I(x, y) = P_0/(\pi \cdot w_x \cdot w_y)$ inside the ellipse and $I(x, y) = 0$ outside, where P_0 is the laser power, and w_x and w_y are radii of ellipse along the x and y axes, respectively. For a Gaussian elliptic beam profile, $I(x, y) = 2P_0/(\pi \cdot w_x \cdot w_y)\exp(-2x^2/w_x^2 - 2y^2/w_y^2)$, where w_x and w_y are the beam waists in x- and y-dimension, respectively. Parameter $K = \alpha T I(0, 0)$ described the extent of bleaching (14).

The time course of fluorescence recovery after photobleaching, $F(t)$, is calculated by integration over (x, y) of the product of $C(x, y, t)$ and probe beam intensity $(q/A)I(x, y)$,

$$F(t) = \frac{q}{A}\int_{-\infty}^{\infty}\int_{-\infty}^{\infty} I(x,y)C(x,y,t)dxdy \qquad (4)$$

Parameter q is the product of the efficiencies of light absorption, emission, and detection, and A is the attenuation factor during observation of recovery. For display of recovery curves, the fractional $f(t)$ was used: $f(t) = [F(t) - F(0)]/[F(\infty) - F(0)]$, where $F(0)$ is initial fluorescence after photobleaching; $F(0) = (qP_0C_0/A)\exp(-K)$ for a uniform elliptic disk and $(qP_0C_0/A)K^{-1}[1-\exp(-K)]$ for a Gaussian elliptic beam, and $F(\infty) = qP_0C_0/A$ is fluorescence at full recovery (14). The $f(t)$ for a uniform circular bleach spot of diameter $2w$ is,

$$f(t) = \exp(-2\tau_D/t)[I_0(2\tau_D/t) + I_1(2\tau_D/t)], \qquad (5)$$

where I_0, I_1 are modified Bessel functions, and $\tau_D = w^2/4D$. (15).

For a uniform elliptical bleach spot, double integrals over the elliptical domain in Eqs. 3 and 4 were calculated by numerical integration. For efficiency in computation we consider the diffusion of bleached molecules out of the spot rather than the diffusion of unbleached molecules into the spot. The concentration $C^*(x, y, t) = C_0 - C(x, y, t)$ was computed numerically with $C^*(x, y, 0) = 0$, reducing the double integral in Eq. 3 to zero outside of the ellipse. Software was written in FORTRAN and was run in a batch process using the GNU FORTRAN G77 compiler to generate $f(t)$ and compute $t_{1/2}$ (time for 50% recovery) (Fig. 2 *A*). The computation was validated by comparing simulated $f(t)$ for a circular spot with the analytical solution (Eq. 5), and showing insensitivity of computed $f(t)$ to a fivefold increases in (x, y) and t resolution.

METHODS

Instrumentation for elliptical spot photobleaching

Photobleaching measurements were done on an apparatus described previously (3,16) with modifications (Fig. 1 *B*). The first-order beam of an argon ion laser (2 W at 488 nm) was diffracted by an acousto-optic modulator and focused onto the surface of the mouse spinal cord or brain through a dichroic mirror (510 nm) and objective lens (Nikon, Tokyo, Japan; 50× air, N. A. 0.55, working distance 8 mm, or 20× air, N. A. 0.35, working distance 20.5 mm). Cylindrical lenses (focal length 20 cm, Thorlabs, Newton, NJ) with vertical or horizontal axes could be introduced into the excitation pathway using a slider, which changed the spot shape from circular to elliptical (axial ratio 1:3) in the focal plane. Emitted fluorescence was filtered (510 nm long pass) and detected by a photomultiplier. Confocal detection was achieved by positioning a 400-μm-diameter precision pinhole (using an *xy* micropositioner) at the back focal plane. Fluorescence was sampled continuously over 200 ms before the bleach pulse, at rates of up to 1 kHz for 0.5–1 s after bleaching, and then at 1 Hz (shutter opened for 20 ms per acquisition) for longer times (10–80 s).

Mice

Experiments were performed on weight-matched (25–30 g) male CD1 and C57/BL6 mice. Protocols were approved by the University of California San Francisco Committee on Animal Research. Mice were anesthetized with 2,2,2-tribromoethanol (avertin, Sigma-Aldrich, St. Louis, MO) (i.p. 125 mg/kg) and core temperature was maintained between 37 and 38°C.

Dye loading

After exposure of intact dura, the skin flaps were held open using a cylindrical dam to create a pocket for dye loading (Fig. 5). The spinal ECS was dye-loaded by 1 h incubation with aCSF ((in millimolar) NaCl, 145; KCl, 4; $MgCl_2$, 1; $CaCl_2$, 2.5; KH_2PO_4, 1; glucose, 10; pH 7.4) containing FITC-dextran (70 kDa, 35 mg/mL). In some experiments, the spinal intracellular compartment was labeled by incubation with calcein-AM (10 μM in aCSF, Molecular Probes, Eugene, OR) for 1 h. After loading, the dural surface was washed with dye-free aCSF, and the dam and skin flaps were removed. Dye loading in the ECS of brain cortex was done as described previously (3,4). Only mice with bilaterally intact hindpaw pain withdrawal reflexes were used.

Fluorescence measurements

For in vivo measurements, the laser spot was focused onto the spinal cord or brain surface. A small (3-mm diameter, 150-μm thick) glass window was transiently positioned on the surface of spinal cord or brain to dampen cardiorespiratory oscillations during measurement (Fig. 1 *B*). The glass window did not affect diffusion measurements (3). Bleaching was accomplished by increasing laser illumination intensity ~4000-fold and bleach duration was set empirically (generally 1–5 ms) to reduce fluorescence by 40–50%. Fluorescence recovery curves with sagittal and transverse orientations of the ellipse were obtained from two to five different spots per condition per mouse. Some measurements were done without the cylindrical lens (giving a circular spot) or with the cylindrical lens at a 45° angle. For in vitro measurements, aCSF solutions containing FITC-dextran (70 kDa, 35 mg/mL) were sandwiched between two glass coverslips or between a diffraction grating (1200 grooves per millimeter) and coverslip (Fig. 4).

Histology

Brain and spinal cord were fixed in 10% formalin, passed through graded ethanols, immersed in Citrisolv (Fisher, Hampton, NH), and embedded in

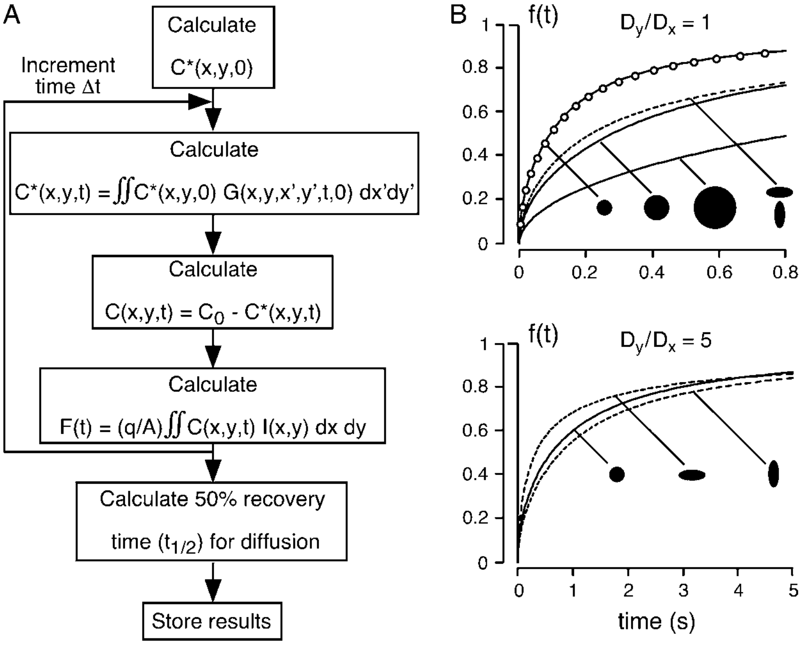

FIGURE 2 Computation of fluorescence recovery curves, $f(t)$. (*A*) Computation involves numerical solution of the diffusion equation in anisotropic media with initial conditions established by bleaching an elliptical spot. See Theory section. (*B*) Calculated fluorescence recovery curves for fluorophore diffusion in isotropic (*top*) and anisotropic (*bottom*) media. (*Top*) Computed $f(t)$ for circular spot (*top line*) is identical to curve obtained from analytical solution of the diffusion equation (*dots*). Curves computed from Eqs. 1–5 with parameters: $K = 1$; $D_x = D_y = 6.25 \times 10^{-7}$ cm^2/s; $w = 5, 8.66, 15$ μm; $w_x = 15$, $w_y = 5$ μm. (*Bottom*) $K = 1$; $D_x = 10^{-7}$ cm^2/s; $D_y = 5 \times 10^{-7}$ cm^2/s; $w = 8.66$ μm; $w_x = 15$, $w_y = 5$ μm.

paraffin. Tissue sections (7-μm thick) were deparaffinized in Citrisolv and rehydrated with graded ethanols. Samples were incubated with a polyclonal rabbit antineurofilament-M antibody (Chemicon, Temecula, CA) and immunoreactivity was visualized using a FITC-labeled goat anti-rabbit antibody.

RESULTS

Computation of diffusional anisotropy from elliptical photobleaching

To confirm the accuracy of the numerical computation, $f(t)$ was computed for isotropic diffusion using a circular bleach spot, for which an analytical solution exists (Eq. 5). Fig. 2 *B* (*top*) shows $f(t)$ for circular spots with three different radii and for elliptical spots (axial ratio 1:3). Computed $f(t)$ (*open cricles*) was in excellent agreement with the analytical solution (*dotted lines*). As predicted, $f(t)$ was not affected by the ellipse orientation when diffusion is isotropic. In contrast, anisotropic diffusion produced marked slowing of fluorescence recovery with the long axis of the ellipse orientated parallel versus perpendicular to the direction of fastest diffusion (Fig. 2 *B*, *bottom*). For comparison, $f(t)$ is shown for a circle with the same area as the ellipses.

Computed $f(t)$ for different diffusion coefficients (D_x and D_y) and ellipse axial ratios allows determination of diffusional anisotropy (D_y/D_x) and absolute diffusion coefficients from measured recovery half-time $t_{1/2}$. Fig. 3 *A* shows ratios of recovery half-times ($t^{(b)}_{1/2}/t^{(a)}_{1/2}$) computed as a function of D_y/D_x for different ellipse axial ratios (with fixed 10-μm short ellipse diameter). As the ellipses become long and thin, $t^{(b)}_{1/2}/t^{(a)}_{1/2}$ approaches D_y/D_x because fluorescence recovery relies more on unidirectional diffusion. For more round ellipses, $t^{(b)}_{1/2}/t^{(a)}_{1/2}$ approaches unity as fluorescence recovery becomes more independent of ellipse orientation. All curves pass through (1,1) as expected. D_y/D_x can thus be deduced from $t_{1/2}$ ratios. Results in Fig. 3 *A* fitted well to the empirical equation: $t^{(b)}_{1/2}/t^{(a)}_{1/2} = (D_y/D_x)^{\gamma}$ ($r^2 = 0.999$), where $\gamma = 0.527$ for the 1:3 elliptical spot (used experimentally here). The maximum deviation of the fitted curve is <4% for $0.1 \leq D_y/D_x \leq 10$. Fig. 3 *B* shows that the determination of absolute D_y and D_x from plots of D_x vs. $t^{(b)}_{1/2}$. Each curve is a rectangular hyperbola corresponding to specified D_y/D_x.

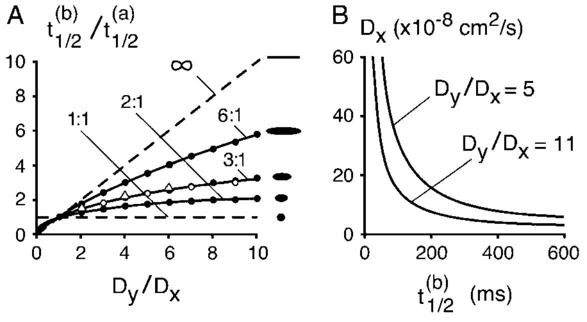

FIGURE 3 Determination of directional diffusion coefficients from fluorescence recovery curves. (*A*) Ratio of fluorescence recovery half-times with ellipse in orientation *b* (long axis in *y*-direction) versus orientation *a* (long axis in *x*-direction), $t^{(b)}_{1/2}/t^{(a)}_{1/2}$, as a function of D_y/D_x. Curves for ellipses with different axis ratio are shown. $K = 1$; $D_x = 10^{-7}$ cm^2/s for $D_y \geq D_x$, $D_y = 10^{-7}$ cm^2/s for $D_y < D_x$; $w_x = 5, 10, 15, 30$ μm; $w_y = 5$ μm. Computations done for flat elliptical illumination profiles; triangles show computed D_y/D_x for a Gaussian beam profile for the 3:1 ellipse. Open circles show results from computations for the 3:1 ellipse done for the exact 3D diffusion case (see Supplementary Material). (*B*) Absolute diffusion coefficients D_x as a function of $t^{(b)}_{1/2}$ for indicated D_y/D_x.

The computation above assumed a flat beam intensity profile in the elliptical area, whereas actual profiles were in-between flat-field and Gaussian distributions (not shown). To examine the sensitivity of the D_y/D_x computation to the assumed illumination profile, simulations were done for the 30 × 10 μm ellipse comparing Gaussian versus flat beam profiles. Fig. 3 *A* shows that simulation with the Gaussian versus flat beam profiles produced nearly identical relations between D_y/D_x and $t^{(b)}_{1/2}/t^{(a)}_{1/2}$. Fig. 3 *A* also shows results from a full 3D computation (*open circles*; see Supplementary Material) in which the diffusion equation in 3D was solved with anisotropic diffusion (for spinal cord, $D_x = D_z$) and reflective boundary conditions at the spinal cord surface, as well as experimentally measured 3D illumination profiles and detection efficiencies for our optical system. Computed $t^{(b)}_{1/2}/t^{(a)}_{1/2}$ vs. (D_y/D_x) for the 3D and 2D computations were in excellent agreement.

Method validation: anisotropic diffusion in vitro

Photobleaching experiments were carried out in aCSF solutions containing 70 kDa FITC-dextran sandwiched between coverslips (Fig. 4 *A*, *top*) using circular (~10-μm diameter) or elliptical (~10- and 30-μm diameters) spots. Under this condition diffusion is isotropic in the *x*,*y* plane ($D_x = D_y$). Fluorescence recovered fully after photobleaching (*middle*), with approximately twofold increase in the half-time, $t_{1/2}$, for the elliptical spot (*bottom*). As expected, recovery was independent of the orientation of the ellipse (not shown). These data agree with the theoretical model (Fig. 3 *A*), predicting a $t^{(\text{ellipse})}_{1/2}/t^{(\text{circle})}_{1/2}$ ratio of 2.2.

To simulate anisotropic diffusion, the FITC-dextran solution was sandwiched between a diffraction grating and coverslip, rendering the parallel grooves of the grating fluorescent (Fig. 4 *B*, *top*). Here, FITC-dextran diffusion occurs along but not across the grooves. Photobleaching was done using a circular spot, and an elliptical spot in three different orientations (*a*–*c*) as depicted. Fluorescence recovery was remarkably slowed when the long axis of the ellipse (orientation *b*) was parallel to the grooves of the grating (*middle*). The $t_{1/2}$ for fluorescence recovery was similar for ellipse *b* versus the circle (*bottom*), but 9- to 10-fold slowed for ellipse *a* versus ellipse *b*. These ratios agree with the theoretical ratios of $t^{(b)}_{1/2}/t^{(\text{circle})}_{1/2} = 1$ and $t^{(b)}_{1/2}/t^{(a)}_{1/2} = 9$.

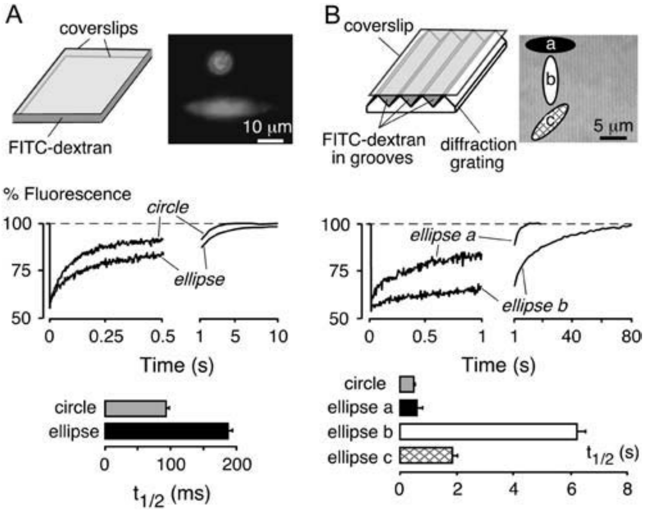

FIGURE 4 Validation of elliptical spot photobleaching. (*A*, *top left*) FITC-dextran sandwiched between coverslips produces an isotropic medium. (*A*, *top right*) Photograph of the circular and elliptical spots. (*Middle*) Representative fluorescence recovery curves after photobleaching with elliptical versus circular spot. (*Bottom*) Summary of recovery half-time $t_{1/2}$ (mean ± SE, $n = 5$–10). (*B*, *top left*) FITC-dextran sandwiched between diffraction grating and coverslip produces an anisotropic medium, where diffusion is possible parallel to the grooves. (*B*, *top right*) Fluorescence micrograph of diffraction grating containing fluorophore dissolved in aCSF. Photobleaching was performed with ellipse in orientations *a*, *b*, and *c*. (*Middle*) Representative fluorescence recovery curves for ellipse *a* versus *b*. *Bottom*. Summary of recovery $t_{1/2}$ (mean ± SE, $n = 5$–10).

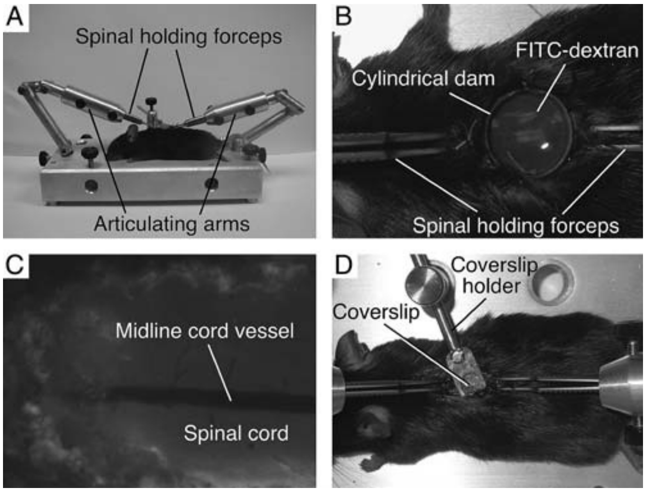

FIGURE 5 Spinal cord preparation for fluorescence measurements. (*A*) After anesthesia and spinal exposure, the mouse spine was immobilized using two pairs of forceps held by articulating arms. (*B*) Dye was loaded in the ECS of spinal cord using a cylindrical dam sutured onto surrounding skin. (*C*) Fluorescence of dye-loaded spinal cord with nonfluorescent blood vessels. (*D*) During recordings, a coverslip gently rested on the spinal cord to dampen cardiorespiratory oscillations.

Anisotropic diffusion in spinal cord in vivo

Experiments were performed after spinal immobilization (Fig. 5 *A*) and dye loading by diffusion through the intact dura (Fig. 5 *B*). Dye loading produced a strong fluorescence signal from the exposed spinal cord, with dark midline vessel and its branches (Fig. 5 *C*). For photobleaching measurements, cardiorespiratory oscillations were damped by resting a glass coverslip gently on the dura (Fig. 5 *D*). Measurements were taken with the elliptical or circular spot focused on a vessel-free area in the region bound medially by the midline vessel and laterally by the dorsal root entry zone.

The dorsal white matter tracts of the spinal cord consist mostly of densely packed myelinated axons orientated rostrocaudally (Fig. 6 *A*). Marked slowing in FITC-dextran fluorescence recovery was found when the long axis of the ellipse was positioned parallel (orientation *b*) versus perpendicular (orientation *a*) to the neuronal axons (Fig. 6 *B*, *left*), indicating faster diffusion in the rostro-caudal versus mediolateral directions. We predicted that diffusional anisotropy would be even greater for a dye that is confined to the cytoplasmic compartment because diffusion can only occur along axons. Fig. 6 *B* (*right*) shows remarkable slowing of fluorescence recovery of cytoplasmic calcein when the long axis of the ellipse was oriented parallel versus across the tract. Ten minutes of anoxia (by anesthetic overdose) greatly impaired diffusion in the ECS (Fig. 6 *A*, *left*) both along and perpendicular to the neuronal fibers.

Fig. 6 *C* summarizes $t_{1/2}$ data for FITC-dextran diffusion in the ECS of spinal cord, and calcein diffusion in the cytoplasm. Averaged $t_{1/2}$ ratios with the long axis of the ellipse orientated across versus along fibers are summarized in Fig. 6 *D*, shown with deduced diffusional anisotropy D_y/D_x. Also shown is FITC-dextran diffusion in isotropic solution (from Fig. 4 *A*) with $D_y/D_x \sim 1$, and under anisotropic conditions (from Fig. 4 *B*) with $D_y/D_x \rightarrow \infty$. There was diffusional anisotropy in both cytoplasm ($D_y/D_x = 11 \pm 4$) and the ECS compartment ($D_y/D_x = 5 \pm 2$) of the dorsal white matter tracts. Cytoplasmic diffusional anisotropy was not infinite probably because of small imperfections in tract alignment, and diffusion in some astroglia aligned perpendicular to the neuronal fibers.

Absolute D_y and D_x were computed from elliptical spot photobleaching for the spinal cord dorsal white matter tracts by plotting D_x vs. $t_{1/2}$ curves corresponding to the D_y/D_x of the cytoplasmic and ECS compartments as explained above (Fig. 6 *E*). Diffusion of FITC-dextran along neuronal fibers was slowed 1.8-fold compared with diffusion in solution (at 37°C), whereas FITC-dextran diffusion across neuronal fibers was slowed by an additional 5.0-fold. In axonal cytoplasm, calcein diffusion along the fibers was 2.3 times slower than diffusion in water.

Isotropic diffusion in brain in vivo

Photobleaching was also done in cerebral cortex in vivo, using elliptical and circular spots. The ECS of brain cortex

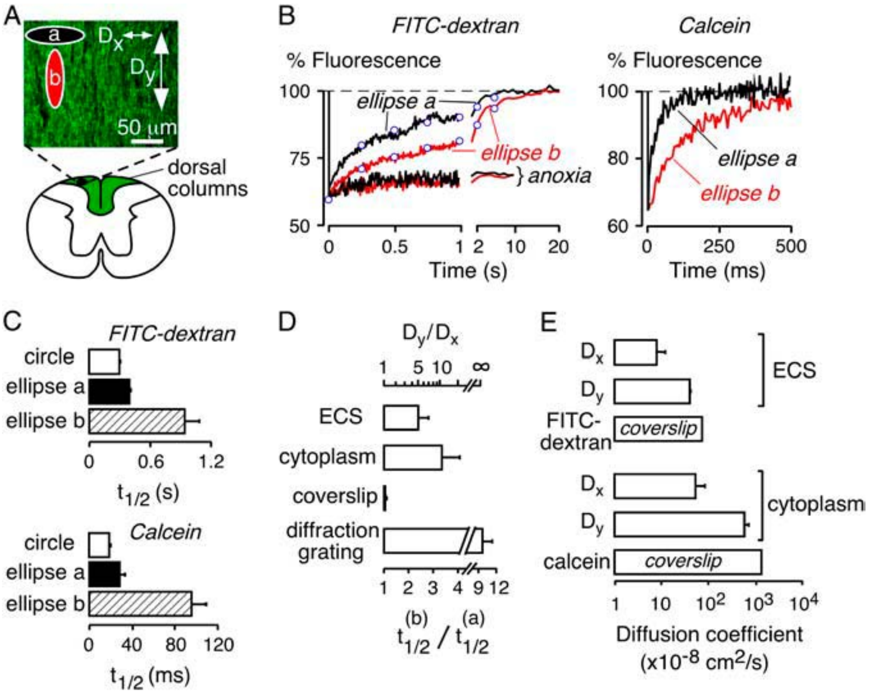

FIGURE 6 Anisotropic diffusion in spinal white matter tracts. (*A*) Spot photobleaching was performed on the dorsal columns viewed from the top, which consist of myelinated axons aligned rostrocaudally (*y* direction); top shows cord section immunostained for neurofilament to reveal axons. Axons appear ''wavy'' due to processing artifact. Spot photobleaching was done with ellipse orientations *a* and *b*. (*B*, *left*) Representative fluorescence recovery curves for FITC-dextran in ECS for ellipse *a* (*black curves*) versus *b* (*red curves*). Blue open circles show computed recovery curves for the 3:1 ellipse with $D_y/D_x = 5$, $D_z = D_x$ for the 3D simulation. Also shown is measurement done after 10 min of anoxia. (*Right*) Recovery curves for calcein in axonal cytoplasm. (*C*) Summary of data for FITC-dextran (mean ± SE, $n = 4$) and calcein ($n = 3$). (*D*) Ratio of $t_{1/2}$ for ellipse *b* versus *a*, and deduced D_y/D_x for FITC-dextran in the ECS and calcein in cytoplasm of spinal cord. Shown for comparison are data for FITC-dextran in isotropic aCSF solution (*coverslip*) and on a diffraction grating. (*E*) Absolute diffusion coefficients for FITC-dextran in ECS versus ''coverslip'', and for calcein in cytoplasm versus ''coverslip''.

was stained with FITC-dextran by craniectomy (without dural trauma), dye loading by diffusion, and dye washing. Histological examination of tangential sections of cerebral cortex revealed a complex arrangement of neuronal fibers lacking directional preponderance (Fig. 7 *A*). Fig. 7, *B* and *C*, show near identical fluorescence recovery after photobleaching when the long axis of the ellipse was positioned rostrocaudally (orientation *a*) versus mediolaterally (orientation *b*) or at 45° (not shown). The ratio $D_y/D_x \sim 1$ (Fig. 7 *D*) confirms isotropic diffusion of FITC-dextran in the ECS of brain cortex. The absolute diffusion coefficient of 2.2×10^{-7} cm^2/s for FITC-dextran diffusion in the ECS (Fig. 7 *D*) is ~3.3-fold slower than that in saline (at 37°C). Assuming that viscosity in brain slows diffusion by 1.8-fold, as found in spinal cord, cerebral cortex ECS geometry (tortuosity) slows ECS diffusion by an additional 1.8-fold.

DISCUSSION

Molecular diffusion in brain ECS is slower than diffusion in water (3,6,17). Here, a novel photobleaching technique was developed to resolve for the first time the relative

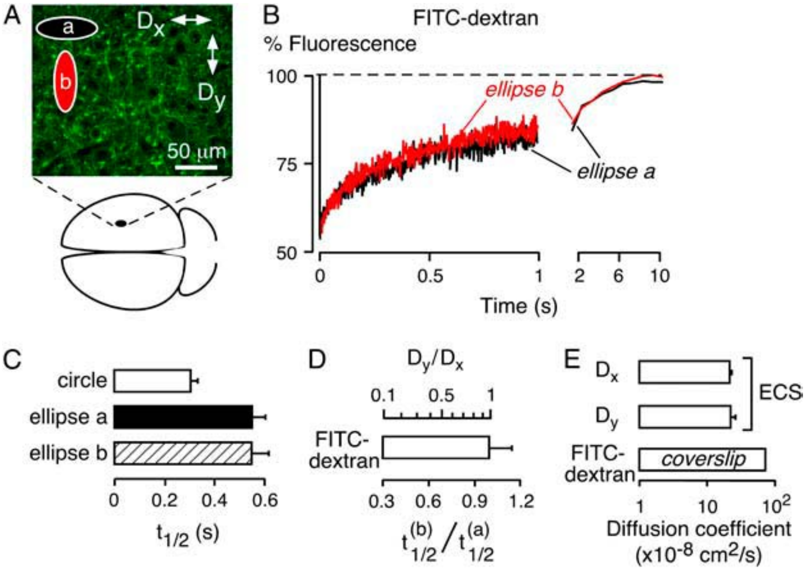

FIGURE 7 Isotropic diffusion in ECS of cerebral cortex. (*A*) Spot photobleaching was done on exposed parietal lobes, which consist of neuronal processes with no directional preponderance; top shows section immunostained for neurofilament. (*B*) Representative fluorescence recovery curves for FITC-dextran diffusion for ellipse *a* versus *b*. (*C*) Data summary (mean ± SE, $n = 3$–6) for bleaching with circle versus ellipses *a* and *b*. (*D*) Ratio of $t_{1/2}$ for ellipse *b* versus *a*, and deduced D_y/D_x. (*E*) Absolute diffusion coefficients for FITC-dextran in ECS versus aCSF (*coverslip*).

contributions of the two major determinants of molecular diffusion in the ECS—viscosity versus geometry/tortuosity. Our method utilized an elliptical spot produced by cylindrical excitation optics to introduce directionality into the measurement. Diffusional anisotropy was deduced from differential rates of photobleaching recovery for parallel and perpendicular orientations of the long axis of the ellipse with respect to the direction of greatest diffusion. Measurement of direction-dependent diffusion was required to resolve viscous versus geometric factors in the highly anisotropic white matter of spinal cord, where diffusion along the tract axis is slowed mainly by viscosity.

The principal finding was that the viscosity modestly slows macromolecular diffusion in the ECS, $\sim$1.8 times compared with diffusion in water. Because the major constituents of ECM (hyaluronic acid and hyaluronic acid binding proteins) are similarly distributed in gray versus white matter (18,19), we assumed that brain and spinal cord ECM hinder diffusion equally. In cerebral cortex, ECS geometry was found to slow diffusion $\sim$1.8-fold, in agreement with theoretical models of packed cells, where geometry was predicted to hinder ECS diffusion 1.5- to 1.9-fold (10,12). The ECM in CNS is rich in glycosaminoglycans and hyaluronan but lacks fibrous components, such as collagen, which are common in peripheral tissues (20). In tumors, collagen but not hyaluronan or glycosaminoglycan content correlated with slowed macromolecular diffusion in ECS; collagenase treatment accelerated but hyaluronidase hindered macromolecular diffusion in tumor ECS (21,22). We propose that the ECM in the CNS has evolved to facilitate rather than hinder diffusion by forming a large-pore medium that maintains cell-cell spacing, which is essential for efficient cell-cell communication.

Diffusion measurements by spot photobleaching and fluorescence correlation spectroscopy (FCS) generally assume isotropic diffusion, although a few studies have considered anisotropy. An attempt was made to measure anisotropic diffusion in skeletal muscle using a rectangular window to follow fluorescence recovery after bleaching a large, circular spot (23); however, no anisotropic diffusion was found. FCS was used to investigate anisotropic diffusion of FITC-dextran in dendrites of mitral cells from *Xenopus* tadpoles (24). Slowed lateral diffusion was interpreted in terms of effects of an oriented dense intradendritic microtubule network. The cylindrical optics described here should also allow measurement of anisotropic diffusion by FCS utilizing autocorrelation functions for elliptical detection volumes.

Our 2D diffusion model yielding an analytical solution was validated by a 3D Monte-Carlo computation, which took into account diffusion in the third dimension with reflective boundary conditions at the surface of the spinal cord, as well as experimentally measured 3D profiles for illumination and detection efficiency. The 2D computation is an excellent approximation here because fluorophore diffusion from below is minimal in spinal white matter where D_z is small ($\sim D_x$). In addition, the confocal optics minimized the z-detection depth, and the objective and cylindrical lenses were chosen to achieve a near-constant cylindrical beam profile for many microns in the z-direction as verified experimentally (see Supplementary Material).

Diffusion measurements were done in spinal cord after laminectomy to expose intact dura, allowing excellent visualization of the intact and pulsatile spinal cord through the thin dural sac (Fig. 5). The hindpaw withdrawal reflexes were also present bilaterally, suggesting preserved functionality. In $<$10% of mice (not used for measurements) hemorrhage was seen on the surface of the spinal cord and the hindlimb pain reflexes became absent. Our technique does not allow the study of surgically inaccessible regions, such as the gray matter located deep in cord tissue, or the spinothalamic and corticospinal tracts that lie anterior and lateral. Deep structures can be accessed using slice preparations. However, we have consistently found faster dextran diffusion in vivo (3,4), compared with data from brain slices obtained using integrative optical imaging (17,25,26). Cell swelling markedly hindered dextran diffusion in vivo (3,4), but only mildly impaired diffusion in brain slices (25). These findings suggest that in slices, baseline ECS geometry is more restrictive than in vivo, which may be due to cellular damage during cutting.

The relative hindrances to ECS diffusion arising from ECS tortuosity versus viscosity were estimated assuming that molecules diffusing rostro-caudally in ECS of the dorsal columns do not circumvent axons, resulting in little or no geometric hindrance to their diffusion. This is supported by histological studies of rodent dorsal columns, which reveal densely packed, cylindrical neuronal fibers orientated parallel to the long axis of the spinal cord with diameters 0.5–2 μm (27,28), well below our circular ($\sim$10-μm diameter) and elliptical ($\sim$30- and $\sim$10-μm diameters) spot sizes.

Diffusion of calcein inside axonal fibers was slowed $\sim$2.3-fold compared with diffusion of calcein in water. Slowing of diffusion by 2.5- to 4-fold has been found for other fluorescein-sized small molecules in cytoplasm of various cultured cells (29) as reviewed by Verkman (30). Molecular crowding was shown to be the principal factor accounting for slowed molecular diffusion in cytoplasm, such that 10–15% crowding by proteins and other macromolecular solutes/structures is predicted to slow diffusion by two- to threefold. Binding of diffusing molecules to slowly moving cytoplasmic components can further slow diffusion, though generally by little for a small polar solute. In cytoplasm of CHO cells, calcein diffusion was slowed approximately fourfold compared to its diffusion in water (31). The lesser fold slowing of calcein diffusion by axonal cytoplasm compared with cytoplasm of round cells is probably due to the alignment of axonal microtubules and neurofilaments, and the low concentration of membraneous structures such as endoplasmic reticulum (32).

Attempts have been made to measure anisotropy with the TMA$^+$ method by using different orientations of the iontophoresis and recording electrodes. However, anisotropies ($D_y/D_x = \lambda_x^2/\lambda_y^2$) were small; only 1.4 in rat corpus callosum in vivo (33), and 1.7 in ECS of rat spinal white matter in vitro (34). There are potential concerns with the application of the TMA^+ method to study anisotropic diffusion, including direct invasion of the measurement site and the directional TMA^+ iontophoresis pulse, both of which could perturb direction-dependent TMA^+ diffusion. In vivo, cardiorespiratory pulsations of CNS tissue may further compromise the ability of the TMA^+ method to detect anisotropic diffusion, whereas in brain slices differential transection of fiber tracts by the cutting procedure may introduce artifactual direction dependence. Also, computation of direction-dependent diffusion coefficients using the TMA^+ method requires multiparameter curve fitting, including diffusion coefficients, extracellular volume fraction, and a correction factor for TMA^+ partitioning into cells. Another method for studying anisotropic diffusion in vivo is diffusion tensor magnetic resonance imaging (35,36). Despite the advantage of noninvasiveness and the ability to image the entire neuraxis, tensor imaging is largely limited to the detection of proton/water diffusion and thus unable to distinguish between intracellular and extracellular compartments.

In summary, we have established and validated a minimally invasive elliptical spot photobleaching method to quantify anisotropic diffusion of fluorescent macromolecules in vivo. Unlike the TMA^+ technique, our method can measure direction-dependent, intra- or extracellular diffusion of a wide range of biologically relevant molecules, such as DNA, proteins, drugs, or liposomes. Anisotropic diffusion or directed motion is anticipated in many biological systems, which have oriented assemblies of barriers, as shown here in spinal cord. Other examples include the layered arrangement of cells in the retina, cerebellar cortex, and striated muscle, as well as the realignment of cytoskeletal fibers, which occurs during cell migration and axonal sprouting. Elliptical spot photobleaching is thus applicable to measurements over distances of many cells, as well as for subcellular diffusion studies when a smaller spot is used.

SUPPLEMENTARY MATERIAL

An online supplement to this article can be found by visiting BJ Online at http://www.biophysj.org.

This work was supported by National Institutes of Health grants EB00415, DK35124, EY13574, HL59198, DK72517, and HL73856 (to A.S.V.). During his tenure in Dr. Verkman's laboratory, M.C.P. was an employee of St. George's, University of London, and was funded by a Wellcome Trust Clinician Scientist Fellowship.

REFERENCES

1. Sykova, E. 2004. Diffusion properties of the brain in health and disease. *Neurochem. Int.* 45:453–466.
2. Zoli, M., C. Torri, R. Ferrari, A. Jansson, I. Zini, K. Fuxe, and L. F. Agnati. 1998. The emergence of the volume transmission concept. *Brain Res. Brain Res. Rev.* 26:136–147.
3. Binder, D. K., M. C. Papadopoulos, P. M. Haggie, and A. S. Verkman. 2004. In vivo measurement of brain extracellular space diffusion by cortical surface photobleaching. *J. Neurosci.* 24:8049–8056.
4. Papadopoulos, M. C., D. K. Binder, and A. S. Verkman. 2005. Enhanced macromolecular diffusion in brain extracellular space in mouse models of vasogenic edema measured by cortical surface photobleaching. *FASEB J.* 19:425–427.
5. Sykova, E., J. Svoboda, J. Polak, and A. Chvatal. 1994. Extracellular volume fraction and diffusion characteristics during progressive ischemia and terminal anoxia in the spinal cord of the rat. *J. Cereb. Blood Flow Metab.* 14:301–311.
6. Hrabetova, S., J. Hrabe, and C. Nicholson. 2003. Dead-space microdomains hinder extracellular diffusion in rat neocortex during ischemia. *J. Neurosci.* 23:8351–8359.
7. Sykova, E., L. Vargova, S. Prokopova, and Z. Simonova. 1999. Glial swelling and astrogliosis produce diffusion barriers in the rat spinal cord. *Glia.* 25:56–70.
8. Roitbak, T., and E. Sykova. 1999. Diffusion barriers evoked in the rat cortex by reactive astrogliosis. *Glia.* 28:40–48.
9. Nicholson, C., and E. Sykova. 1998. Extracellular space structure revealed by diffusion analysis. *Trends Neurosci.* 21:207–215.
10. Rusakov, D. A., and D. M. Kullmann. 1998. Geometric and viscous components of the tortuosity of the extracellular space in the brain. *Proc. Natl. Acad. Sci. USA.* 95:8975–8980.
11. Zamecnik, J., L. Vargova, A. Homola, R. Kodet, and E. Sykova. 2004. Extracellular matrix glycoproteins and diffusion barriers in human astrocytic tumours. *Neuropathol. Appl. Neurobiol.* 30:338–350.
12. Tao, L., and C. Nicholson. 2004. Maximum geometrical hindrance to diffusion in brain extracellular space surrounding uniformly spaced convex cells. *J. Theor. Biol.* 229:59–68.
13. Carslaw, H. S., and J. C. Jaeger. 1997. The use of sources and sinks in cases of variable temperature. *In* Conduction of Heat in Solids. 2nd Ed. Oxford University Press, Oxford, UK. 256–258.
14. Axelrod, D., D. E. Koppel, J. Schlessinger, E. Elson, and W. W. Webb. 1976. Mobility measurement by analysis of fluorescence photobleaching recovery kinetics. *Biophys. J.* 16:1055–1069.
15. Soumpasis, D. M. 1983. Theoretical analysis of fluorescence photobleaching recovery experiments. *Biophys. J.* 41:95–97.
16. Jayaraman, S., N. S. Joo, B. Reitz, J. J. Wine, and A. S. Verkman. 2001. Submucosal gland secretions in airways from cystic fibrosis patients have normal [Na(+)] and pH but elevated viscosity. *Proc. Natl. Acad. Sci. USA.* 98:8119–8123.
17. Nicholson, C., and L. Tao. 1993. Hindered diffusion of high molecular weight compounds in brain extracellular microenvironment measured with integrative optical imaging. *Biophys. J.* 65:2277–2290.
18. Bignami, A., M. Hosley, and D. Dahl. 1993. Hyaluronic acid and hyaluronic acid-binding proteins in brain extracellular matrix. *Anat. Embryol. (Berl.).* 188:419–433.
19. Bignami, A., R. Asher, and G. Perides. 1992. The extracellular matrix of rat spinal cord: a comparative study on the localization of hyaluronic acid, glial hyaluronate-binding protein, and chondroitin sulfate proteoglycan. *Exp. Neurol.* 117:90–93.
20. Novak, U., and A. H. Kaye. 2000. Extracellular matrix and the brain: components and function. *J. Clin. Neurosci.* 7:280–290.
21. Pluen, A., Y. Boucher, S. Ramanujan, T. D. McKee, T. Gohongi, E. di Tomaso, E. B. Brown, Y. Izumi, R. B. Campbell, D. A. Berk, and R. K. Jain. 2001. Role of tumor-host interactions in interstitial diffusion of macromolecules: cranial vs. subcutaneous tumors. *Proc. Natl. Acad. Sci. USA.* 98:4628–4633.
22. Netti, P. A., D. A. Berk, M. A. Swartz, A. J. Grodzinsky, and R. K. Jain. 2000. Role of extracellular matrix assembly in interstitial transport in solid tumors. *Cancer Res.* 60:2497–2503.

23. Papadopoulos, S., V. Endeward, B. Revesz-Walker, K. D. Jurgens, and G. Gros. 2001. Radial and longitudinal diffusion of myoglobin in single living heart and skeletal muscle cells. *Proc. Natl. Acad. Sci. USA.* 98:5904–5909.
24. Gennerich, A., and D. Schild. 2002. Anisotropic diffusion in mitral cell dendrites revealed by fluorescence correlation spectroscopy. *Biophys. J.* 83:510–522.
25. Tao, L. 1999. Effects of osmotic stress on dextran diffusion in rat neocortex studied with integrative optical imaging. *J. Neurophysiol.* 81:2501–2507.
26. Thorne, R. G., S. Hrabetova, and C. Nicholson. 2004. Diffusion of epidermal growth factor in rat brain extracellular space measured by integrative optical imaging. *J. Neurophysiol.* In press.
27. Gerke, M. B., and M. B. Plenderleith. 2004. Analysis of the unmyelinated primary sensory neurone projection through the dorsal columns of the rat spinal cord using transganglionic transport of the plant lectin Bandeiraea simplicifolia I-isolectin B4. *J. Neurol. Sci.* 221:69–77.
28. Li, S., and P. K. Stys. 2000. Mechanisms of ionotropic glutamate receptor-mediated excitotoxicity in isolated spinal cord white matter. *J. Neurosci.* 20:1190–1198.
29. Kao, H. P., J. R. Abney, and A. S. Verkman. 1993. Determinants of the translational mobility of a small solute in cell cytoplasm. *J. Cell Biol.* 120:175–184.
30. Verkman, A. S. 2002. Solute and macromolecule diffusion in cellular aqueous compartments. *Trends Biochem. Sci.* 27:27–33.
31. Solenov, E., H. Watanabe, G. T. Manley, and A. S. Verkman. 2004. Sevenfold-reduced osmotic water permeability in primary astrocyte cultures from AQP-4-deficient mice, measured by a fluorescence quenching method. *Am. J. Physiol. Cell Physiol.* 286:C426–C432.
32. Pannese, E. 1994. Neurocytology: Fine Structure of Neurons, Nerve Processes, and Neuroglial Cells. Thieme Medical Publishers, New York, NY.
33. Vorisek, I., and E. Sykova. 1997. Evolution of anisotropic diffusion in the developing rat corpus callosum. *J. Neurophysiol.* 78:912–919.
34. Prokopova, S., L. Vargova, and E. Sykova. 1997. Heterogeneous and anisotropic diffusion in the developing rat spinal cord. *Neuroreport.* 8:3527–3532.
35. Clark, C. A., and D. J. Werring. 2002. Diffusion tensor imaging in spinal cord: methods and applications: a review. *NMR Biomed.* 15:578–586.
36. Clark, C. A., T. R. Barrick, M. M. Murphy, and B. A. Bell. 2003. White matter fiber tracking in patients with space-occupying lesions of the brain: a new technique for neurosurgical planning? *Neuroimage.* 20:1601–1608.